

# Direct Detection of CDM Substructure

N. Dalal<sup>1</sup> and C.S. Kochanek<sup>2</sup>

<sup>1</sup>Physics Dept., UCSD 0350, 9500 Gilman Dr., La Jolla CA 92093

<sup>2</sup>Harvard-Smithsonian Center for Astrophysics, 60 Garden St., Cambridge, MA 02138  
email: ndalal@ucsd.edu, ckochanek@cfa.harvard.edu

## ABSTRACT

We devise a method to measure the abundance of satellite halos in gravitational lens galaxies, and apply our method to a sample of 7 lens systems. After using Monte Carlo simulations to verify the method, we find that substructure comprises  $f_{sat} = 0.02$  (median,  $0.006 < f_{sat} < 0.07$  at 90% confidence) of the mass of typical lens galaxies, in excellent agreement with predictions of CDM simulations. We estimate a characteristic critical radius for the satellites of  $0''.0001 < b < 0''.006$  (90% confidence). For a  $dn/dM \propto M^{-1.8}$  ( $M_{low} < M < M_{high}$ ) satellite mass function, the critical radius provides an estimate that the upper mass limit is  $10^6 M_{\odot} \lesssim M_{high} \lesssim 10^9 M_{\odot}$ . Our measurement confirms a generic prediction of CDM models, and may obviate the need to invoke alternatives to CDM like warm dark matter or self-interacting dark matter.

*Subject headings:* cosmology: theory – galaxies: formation – gravitational lensing – large-scale structure of universe – dark matter

## 1. Introduction

A discrepancy between the number of satellite halos expected from CDM simulations and the observed numbers of Galactic satellite galaxies is part of the prosecution's case for a crisis in the CDM scenario for structure formation (e.g. Kauffmann 1993, Moore et al. 1999, Klypin et al. 1999). Suggested solutions range from the mundane, such as the inhibition of star formation in the satellites by photoionization (e.g. Klypin et al. 1999, Bullock, Kravtsov & Weinberg 2000), to the exotic, such as the disruption of the satellites by self-interacting dark matter (e.g. Spergel & Steinhardt 2000) or changes in the power spectrum (e.g. Bode, Ostriker & Turok 2001, Colin, Avila-Reese & Valenzuela 2000). The satellite crisis must also be closely related to the more general problem that the number of low luminosity galaxies diverges only as  $1/L \sim 1/M$  while the number of CDM halos diverges as  $\sim 1/M^2$ , implying that the probability of forming a visible galaxy in a low mass halo must diminish as  $\sim M$  (e.g. Scoccimarro et al. 2001, Kochanek 2001, Chiu, Gnedin & Ostriker 2001). In principle, the measured abundances of satellite halos should provide a strong test of the CDM scenario, but because the satellites used as evidence for a problem have low luminosities and (in many cases) low surface brightness, it is difficult to apply

this test to any galaxy besides our own. Moreover, the test only considers the numbers of satellites with detectable optical emission, which is at best a lower bound on the number of CDM halos.

Gravitational lensing is the only probe which avoids both of these limitations, as was already noted by Moore et al. (1999). First, the test can be applied to many lens systems spanning a range of redshifts and physical properties. Second, because lensing phenomena couple directly to mass, lenses are sensitive to both luminous and dark substructures in CDM halos. Mao & Schneider (1998) pointed out that the anomalous image flux ratios observed in several lenses, particularly B1422+231, could be explained by substructures such as low mass satellites in the primary lens galaxy. The primary lens magnifies the perturbations from the substructure, making the brightest images particularly susceptible to the effects of substructure. Recently, Metcalf & Madau (2001) quantified the effects of CDM satellites using simulations and found that the effects should be readily detected, and Chiba (2001) demonstrated that plausible CDM satellite distributions could explain the anomalous flux ratios in B1422+231 and PG1115+080. Detailed studies of B1422+231 (Keeton 2002, Bradac et al. 2002) find that the observed perturbations require substructure with mass scales comparable to CDM substructure ( $\gtrsim 10^6 M_\odot$ ) rather than stellar microlensing, and Metcalf & Zhao (2002) have shown that the anomalous flux ratios cannot be reproduced in a large family of smooth potentials for the primary lens.

The missing link is an approach for analyzing the gravitational lens data to estimate the properties of the satellite population. In this paper we develop such an analysis method and apply it to a sample of 7 lenses to estimate the surface density and characteristic mass of the perturbing satellites. We focused on analyzing four-image radio lenses because using the radio lenses eliminates the problem of dust extinction, and minimizes the problems from stellar microlensing due to the relatively large source size (see Koopmans & de Bruyn 2000). We analyzed the lenses MG0414+0534 (Hewitt et al. 1992), B0712+472 (Jackson et al. 1998), PG1115+080 (Weymann et al. 1980), B1422+231 (Patnaik et al. 1992), B1608+656 (Fassnacht et al. 1996), B1933+503 (Sykes et al. 1998) and B2045+265 (Fassnacht et al. 1999). Of these 7 four-image lenses, 6 show anomalous flux ratios which might be due to the effects of substructure. We develop our formalism, characterize our model for the satellite distribution and test our analysis methods in §2. We apply it to the lens sample in §3. In §4 we review our conclusions and their limitations and then outline the observations needed to improve them.

## 2. Analyzing the Effects of Substructure on Gravitational Lenses

In this section we outline our mathematical approach to analyzing the lenses to determine the properties of the substructure (§2.1) and the physical model we use for the satellites composing the substructure (§2.2). In §2.3 we discuss the relationship between our model and the physical properties of the substructure such as its fractional surface density, mass and velocity scales and linear sizes. In §2.4 we outline our Monte Carlo models and test the analysis method.

## 2.1. A Linearized Approach to Analyzing Substructure

Unlike the primary lens galaxy, which we can observe directly to determine its position and optical properties (e.g. Lehar et al. 2000, Kochanek et al. 2000), we can detect substructure only through its effects on the positions and fluxes of the lensed images. This means that estimates for the properties of the substructure will be difficult to separate from the properties of the primary lens (the “macro” model to adopt the language of the quasar microlensing literature) because many perturbations will be degenerate with changes in the macro model. For this reason, Mao & Schneider (1998) focused on merging image pairs where macro models must generically predict similar image fluxes but the observations sometimes find very different fluxes. We will instead allow the macro model to compensate for the effects of substructure as part of our analysis. If we confine our analysis to typical four-image (two-image) lenses we have 14 (8) constraints for determining the 10 parameters of a realistic macro lens model. For a four-image lens, the macro model is overconstrained and we can attempt to estimate the properties of the substructure. Because we have typically found that it is relatively easy to fit image positions and hard to fit flux ratios using standard lens models, we expect the deflection perturbations from substructure to be small or degenerate with the parameters of the macro model, and the magnification perturbations to be larger and non-degenerate.

We model the lens by combining a macro lensing potential  $\phi(\mathbf{x}, \mathbf{p})$  defined by a set of parameters  $\mathbf{p}$ , with a localized perturbing potential for each image  $\delta\phi_i(\mathbf{x})$ . For later notational simplicity, the source position and flux are considered part of the parameter vector  $\mathbf{p}$ . The time delay surface near image  $i$  is

$$\tau = \frac{1}{2}(\mathbf{u} - \mathbf{x})^2 - \phi(\mathbf{x}, \mathbf{p}) - \delta\phi_i(\mathbf{x}) = \tau_0(\mathbf{x}, \mathbf{p}) - \delta\phi_i(\mathbf{x}), \quad (1)$$

and we find images at solutions of  $\nabla\tau = 0$  with an inverse magnification tensor of  $\mathbf{M}^{-1} = \nabla\nabla\tau$  and magnification  $M = |\mathbf{M}|$  (see Schneider, Ehlers & Falco 1992).

We assume the substructure produces small perturbations, so we can simplify its effects by expanding the lens equations as a linear perturbations to a macro model for each image  $i$ . We would like to linearize the equations so that the process of adjusting the macro models to compensate for the effects of substructure can be done rapidly. For macro parameters  $\mathbf{p}_0$  we find images at positions  $\mathbf{x}_i^{(0)}$  with magnification tensors  $\mathbf{M}_i^{(0)}$  at the solutions to  $\nabla\tau_0(\mathbf{x}_i^{(0)}, \mathbf{p}_0) = 0$ . Expanding the lens equations about these solutions, the perturbed image positions are

$$\mathbf{x}_i^{(1)} = \mathbf{x}_i^{(0)} + \mathbf{M}_i^{(0)} \cdot (\delta\mathbf{x}_i - \Delta\mathbf{p} \cdot \mathbf{C}_i) \quad (2)$$

where  $\delta\mathbf{x}_i = \nabla\delta\phi_i$  is the deflection produced by the substructure and

$$\mathbf{C}_i = \frac{d\nabla\tau_0}{d\mathbf{p}} \quad (3)$$

evaluated at  $\mathbf{x} = \mathbf{x}_i^{(0)}$  and  $\mathbf{p} = \mathbf{p}_0$  is the change in the macro model deflections produced by a

small change  $\Delta \mathbf{p} = \mathbf{p} - \mathbf{p}_0$  in the macro model parameters. The perturbed image magnification is

$$M^{(1)} = M^{(0)} + \frac{dM}{d\delta \mathbf{M}} \cdot \delta \mathbf{M} + \frac{dM}{d\mathbf{p}} \cdot \Delta \mathbf{p} + \frac{dM}{d\mathbf{x}} \cdot \Delta \mathbf{x} \quad (4)$$

which becomes

$$M^{(1)} = M^{(0)} (1 + \delta m_i + \Delta \mathbf{p} \cdot \mathbf{D}'_i + \delta \mathbf{x}_i \cdot \mathbf{E}_i) \quad (5)$$

where

$$\delta m_i = -\text{tr}(\mathbf{M} \delta \mathbf{M}_i^{-1}) \quad \text{for} \quad \delta \mathbf{M}_i^{-1} = -\nabla \nabla \delta \phi_i, \quad (6)$$

is the perturbation in the magnification due to the effects of the substructure on the magnification tensor,

$$\mathbf{D}'_i = \frac{1}{M} \left( \frac{dM}{d\mathbf{p}} - \frac{dM}{d\mathbf{x}} \cdot \mathbf{M} \cdot \mathbf{C} \right) \quad (7)$$

is the perturbation due to changing the lens parameters, and

$$\mathbf{E} = \frac{1}{M} \frac{dM}{d\mathbf{x}} \cdot \mathbf{M} \quad (8)$$

is the perturbation due to the effects of substructure on the deflections. The functions  $\delta m_i$ ,  $\mathbf{D}'_i$  and  $\mathbf{E}$  are all evaluated at  $\mathbf{x} = \mathbf{x}_i^{(0)}$  and  $\mathbf{p} = \mathbf{p}_0$ . The flux of image  $i$  is  $f_i = f_s M_i = f_i^{(0)} (1 + \Delta f) M_i$ , which we can linearize as

$$f_i^{(1)} = f_i^{(0)} (1 + \delta m_i + \Delta \mathbf{p} \cdot \mathbf{D}_i + \delta \mathbf{x}_i \cdot \mathbf{E}_i) \quad (9)$$

where  $\Delta \mathbf{p} \cdot \mathbf{D}_i = \Delta \mathbf{p} \cdot \mathbf{D}'_i + \Delta f$  and the fractional change in the source flux  $\Delta f$  is considered one of the model parameters  $\mathbf{p}$ .

We detect substructure as residuals in fits to the lens parameters which cannot be modeled by the macro potential. If we use a  $\chi^2$  statistic, the fit statistic for the image positions is

$$\chi_a^2 = \sum_{i=1}^N \left( \frac{\mathbf{x}_i^{obs} - \mathbf{x}_i^{(0)} - \mathbf{M}_i^{(0)} (\delta \mathbf{x}_i - \Delta \mathbf{p} \cdot \mathbf{C}_i)}{\sigma_a} \right)^2 \quad (10)$$

where  $\sigma_a \simeq 0''.003$  is the uncertainty in the observed image positions  $\mathbf{x}_i^{obs}$ . The fit statistic for the image fluxes is

$$\chi_f^2 = \sum_{i=1}^N \left( \frac{f_i^{obs} - f_i^{(0)} (1 + \delta m_i + \Delta \mathbf{p} \cdot \mathbf{D} + \delta \mathbf{x}_i \cdot \mathbf{E}_i)}{\sigma_{f,i}} \right)^2 \quad (11)$$

for observed fluxes  $f_i^{obs}$  and flux uncertainties  $\sigma_{f,i} \simeq 0.05 f_i^{obs}$ . The lens position, if measured, is constrained by  $\chi_l^2 = (\mathbf{x}_l^{obs} - \mathbf{x}_l^{(0)} - \Delta \mathbf{p}_l)^2 / \sigma_l^2$  where  $\Delta \mathbf{p}_l$  represents the perturbations to the lens position and  $\sigma_l \simeq 0''.003$  is the uncertainty in the observed position  $\mathbf{x}_l^{obs}$ . Because all the terms entering the fit statistic depend only linearly on the  $\Delta \mathbf{p}$ , the fit statistic is a quadratic of the form  $\chi^2 = \chi_0^2 + 2\Delta \mathbf{p} \cdot \mathbf{I} + \Delta \mathbf{p} \cdot \mathbf{J} \cdot \Delta \mathbf{p}$  which is minimized for  $\Delta \mathbf{p} = -\mathbf{J}^{-1} \cdot \mathbf{I}$  with value  $\chi_{min}^2 = \chi_0^2 - \mathbf{I} \cdot \mathbf{J}^{-1} \cdot \mathbf{I}$ . If the macro model were held fixed, the goodness of fit would be  $\chi_0^2$ ,

combining the effects of the substructure with the differences between the observations and the initial macro model. After adjusting the macro model, the correction  $\Delta\chi^2 = \mathbf{I} \cdot \mathbf{J}^{-1} \cdot \mathbf{I}$  represents the ability of the macro model to mimic the effects of substructure.

In order to test the CDM predictions for substructure we need to estimate the statistical properties of the substructure rather than discuss the evidence for perturbations from substructure in individual lenses. For a statistical model of the substructure characterized by parameters  $\mathbf{s}$ , the probability of the  $\alpha$ th substructure realization for lens  $j$ ,  $\delta_{\alpha j}$ , is  $P(\delta_{\alpha j}|\mathbf{s})$ . Given a concrete model for the substructure  $\delta_{\alpha j}$  we can compute the likelihood for fitting the data as the likelihood of obtaining the  $\chi^2$  statistic we find after reoptimizing the macro lens model given the substructure realization,  $P(D_j|\delta_{\alpha j})$ . The Bayesian probability of the model parameters given the data for  $j = 1 \cdots N$  lenses is

$$P(\mathbf{s}, \delta_{\alpha j}|D_j) \propto P(\mathbf{s})\Pi_{j=1}^N P(D_j|\delta_{\alpha j})P(\delta_{\alpha j}|\mathbf{s}) \quad (12)$$

where  $P(\mathbf{s})$  is the prior probability distribution of the  $\mathbf{s}$ . As in all Bayesian probabilities, the expression summed over all variables is normalized to unity. In estimating the statistical properties of the substructure, we are not interested in the likelihoods of the individual realizations, but in the marginalized distribution

$$P(\mathbf{s}|D_j) \propto P(\mathbf{s})\Pi_{j=1}^N \sum_{\alpha=1}^M P(D_j|\delta_{\alpha j})P(\delta_{\alpha j}|\mathbf{s}) \quad (13)$$

where we sum over the  $\alpha = 1 \cdots M$  Monte Carlo realizations of the substructure for each lens. Typically we used  $M = 10^5$  realizations. As we vary the statistical properties of the substructure  $\mathbf{s}$ , the fraction of the realizations  $\delta_{\alpha j}$  which significantly improve the goodness of fit varies. These changes in the fraction of realizations which improve the fit relative to the macro model alone allow us to estimate the parameters  $\mathbf{s}$  describing the substructure.

In our final analysis we used random realizations of perturbing satellites to estimate the perturbations. It is worth mentioning, however, that the problem can be fully linearized if we use a Gaussian model for the perturbations. If  $\mathbf{k} = \{\delta m_i, \delta \mathbf{x}_i\}$  is a  $d$ -dimensional vector of the perturbation variables, and they have a covariance matrix  $\mathbf{V}^{-1} = \langle \mathbf{k}^T \mathbf{k} \rangle$ , then the Gaussian model for the probability distribution of the perturbations is

$$P(\mathbf{k}) = |\mathbf{V}|^{1/2} (2\pi)^{-d/2} \exp\left(-\frac{1}{2}\mathbf{k} \cdot \mathbf{V} \cdot \mathbf{k}\right). \quad (14)$$

The matrix  $\mathbf{V}$  is proportional to the inverse of the satellite surface density, so by combining eqns. (10), (11) (13) and (14), the marginalizing integrals over the shifts in the lens model and the distribution of satellite realizations can be done analytically using standard methods for linear algebra and Gaussian integrals to leave an expression depending only on the statistical properties of the substructure. We did not use this for our actual analysis because it was relatively easy to perform the necessary Monte Carlo realizations and integrals needed to reproduce the true probability distribution for the substructure and its correlations, but we did use it as an internal check on our results. We mention it here because other studies may find it to be of similar utility.

## 2.2. Substructure Models

Before applying the above formalism to observed lens systems, it is necessary to calculate the expected amplitude of perturbations to lensed images from CDM substructure. This involves calculating the expected levels of astrometric shifts in the image positions, and the RMS fluctuations in the local convergence and shear. These quantities are then magnified by the local magnification tensor of the smooth macro-model.

We model CDM substructure by randomly laying down subclumps of surface density. The substructures seen in CDM simulations appear to have mass profiles consistent with the ‘universal’ NFW profile, however for simplicity we will treat them as pseudo-Jaffe models (density  $\rho \propto r^{-2}(r^2 + a^2)^{-1}$ , see Munoz, Kochanek & Keeton 2001), with convergence, the surface density in units of the critical surface density,

$$\kappa(r) = \frac{\Sigma}{\Sigma_c} = \frac{b}{2} \left[ \frac{1}{r} - \frac{1}{(r^2 + a^2)^{1/2}} \right] \quad (15)$$

where the critical surface density for lensing is  $\Sigma_c = c^2 D_{OS}/4\pi G D_{OL} D_{LS}$ . Here,  $b$  is a length scale similar to the Einstein radius of the subclump, and  $a$  is a tidal or break radius. Note that  $b$ ,  $r$  and  $a$  are angular lengths, which are related to physical sizes by multiplication by the distance to the lens  $D_{OL}$ . The total mass of a clump is  $M = \pi b a \Sigma_c$  where  $\Sigma_c$  is the critical density in angular units. If the surface mass density of the perturbers is  $\Sigma$ , the number of perturbers per unit area is  $N = (\Sigma/\Sigma_c)/\pi b a$ . To leading order, the variance in the image deflection, convergence and shear are

$$\langle |\delta \mathbf{x}|^2 \rangle \simeq \frac{3}{2} \frac{\Sigma}{\Sigma_c} b a \quad \langle \kappa^2 \rangle \simeq \langle \gamma^2 \rangle \simeq \frac{1}{2} \frac{\Sigma}{\Sigma_c} \frac{b}{a} \ln \frac{a}{s} \quad (16)$$

where we must introduce a core radius  $s$  to make the variance in the convergence and shear finite. These perturbations may then be magnified by the macro model to produce the observed perturbations in the image positions and fluxes. If the scale  $a$  is determined by the satellite’s tidal radius, we have  $a = (b b_0)^{1/2}$  where  $b_0$  is the critical radius of the primary lens (see e.g. Metcalf & Madau 2001). Thus, for a fixed satellite surface density, the variance of the astrometry perturbation in units of the critical radius of the macro lens is roughly

$$\frac{\langle |\delta \mathbf{x}|^2 \rangle^{1/2}}{b_0} \simeq 10^{-3} \left( \frac{10 \Sigma}{\Sigma_c} \right)^{1/2} \left( \frac{10^3 b}{b_0} \right)^{3/4}, \quad (17)$$

while the variance in the shear and convergence is roughly

$$\langle \kappa^2 \rangle^{1/2} \simeq \langle \gamma^2 \rangle^{1/2} \simeq 0.13 \left( \frac{10 \Sigma}{\Sigma_c} \right)^{1/2} \left( \frac{10^3 b}{b_0} \right)^{1/4} \left( \frac{\ln \Lambda}{10} \right)^{1/2} \quad (18)$$

where  $\ln \Lambda = \ln(\sqrt{b b_0}/s) \sim 10$ .

### 2.3. Physical Scales and Interpretations

For this first attempt at modeling substructure, we consider satellites with constant surface density  $\Sigma/\Sigma_c$  and critical radius  $b$ . We scale the satellite break radius like a tidal radius with  $a = (bb_0)^{1/2}$  for  $b_0 \equiv 1''0$ . Near the critical radius of a moderately elliptical isothermal lens the surface density is  $\Sigma_c/2$ , so the projected satellite mass fraction is  $f_{sat} = 2\Sigma/\Sigma_c$ . In the cylinder (sphere) defined by the Einstein radius, roughly 50% (10%) of the mass is dark matter (see, e.g., Keeton 2001b). The Einstein ring, where we make the measurement, is typically 1.0-1.5 effective radii from the lens center and the dark matter fraction will be significantly higher than these average values at the edge of the cylinder where we see the images. Hence, we can interpret  $f_{sat}$  as the fraction of the dark matter near the Einstein ring in substructure with only modest baryonic corrections.

We use only observational parameters in our models, which means that the physical parameters will have small shifts between the lenses we consider because of the changing lens and source distances. To provide a sense of the physical scales, consider the parameters for PG1115+080 with source and lens redshifts of  $z_s = 1.72$  and  $z_l = 0.31$  respectively. The inner circular velocity of a satellite is  $v_{circ} = 9.7(b/0''.001)^{1/2}$  km/s, and its mass is  $M = 3.4(b/0''.001)^{3/2} \times 10^6 h^{-1} M_\odot$ . The angles  $b$  and  $a$  correspond to proper distances of  $3(b/0''.001)h^{-1}$  pc and  $100(b/0''.001)^{1/2}h^{-1}$  pc compared to the average distance of  $1''.16$  or  $3.6h^{-1}$  kpc of the images from the lens center. For the other lenses, the distances scale linearly with  $D_{OL}$ , the circular velocity scales as  $(D_{LS}/D_{OS})^{-1/2}$  and the mass scales as  $D_{OS}/D_{OL}D_{LS}$ . These changes between lenses are sufficiently small compared to our logarithmic uncertainties to ignore.

We will use satellites with fixed properties in our models, so our estimate of the mass scale is a weighted average of the satellite masses. Given our statistical uncertainties models with a mass spectrum are unwarranted, and we should be able to estimate the effects of using a mass spectrum simply by matching the variance in the shear and astrometry perturbations (Eqn. 16). The mass function of the satellite halos is  $dN/dM \propto M^{-\alpha}$  with  $1.7 \lesssim \alpha \lesssim 1.8$  (e.g. Moore et al. 1999, Klypin et al. 1999, Metcalf & Madau 2001, Springel et al. 2001, Helmi et al. 2002) which we limit to a finite range  $M_{low} < M < M_{high}$  to avoid divergences in the total mass. With  $\alpha < 2$ , only the upper mass limit is important in estimating the perturbations. Our effective substructure mass  $M$  is related to the upper mass limit by  $M = M_{high}(2 - \alpha)/(3 - \alpha) = M_{high}/6$  if we match the amplitude of the astrometry perturbations and by  $M = M_{high}((2 - \alpha)/(7/3 - \alpha))^3 = M_{high}/20$  if we match the shear perturbations. Given the precision with which we can currently estimate the characteristic mass scale, we choose not to include a satellite mass function. Crudely, we can estimate that  $M_{high} \sim 10 - 20M$ .<sup>1</sup>

---

<sup>1</sup>For  $\alpha = 2$  the results become logarithmically sensitive to the lower mass limit. If we match the astrometric perturbations, our mass scale corresponds to  $M = M_{high}/\ln C \simeq M_{high}/10$  where  $C = M_{high}/M_{low}$  is the ratio of the upper and lower mass limits. If we match the shear perturbations, assuming the Coulomb logarithm is held fixed, our mass scale corresponds to  $M = M_{high}(3/\ln C)^3 \sim M_{high}/30$ .

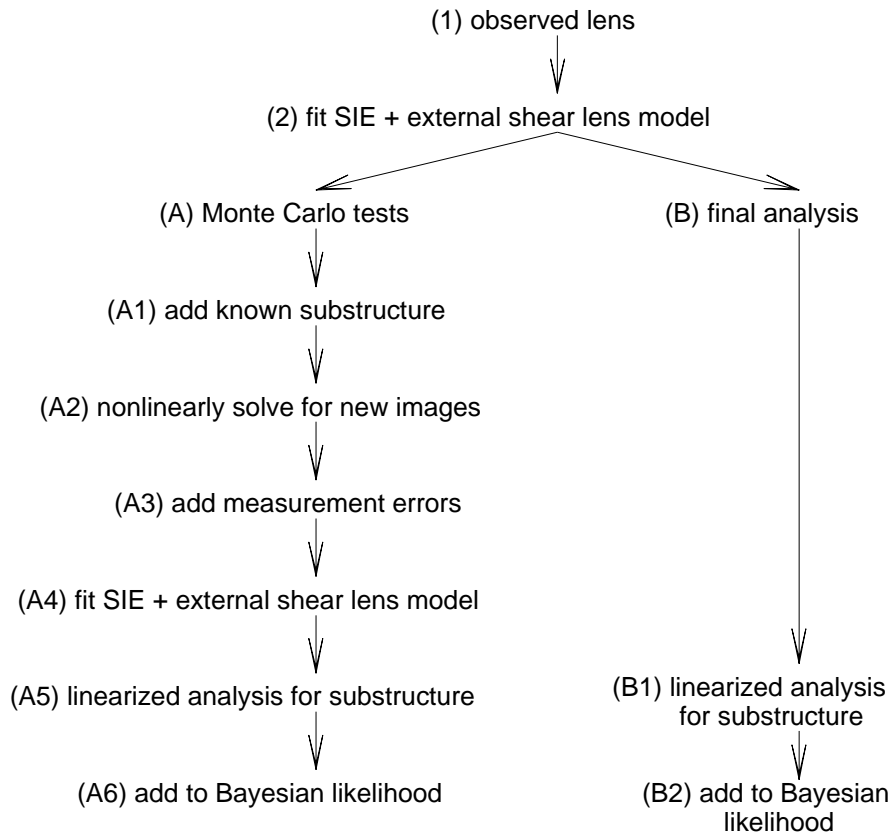


Fig. 1.— Outline of analysis procedures.



## 2.4. Analysis Procedures and Monte Carlo Tests

In Fig. 1 we outline our procedures for analyzing the lens data and for testing our method to ensure that it can recover the properties of the substructure accurately by following the treatment we use for each lens in the sample. We start (#1) with the available data on the lens. The first processing step (#2) is to model the lens with the *lensmodel* package (Keeton 2001a) using singular isothermal ellipsoids (SIE) in external shear fields for the mass distribution of the primary lens galaxy. The SIE model is the only standard lens model which is consistent with general properties of the lens sample (see, e.g. Cohn et al. (2001), and references therein). Where needed, we added additional SIE lens components so as to reproduce the best standard models for each system. We used the observed astrometric uncertainties but broadened the uncertainties in the flux ratios to 20% to compensate for systematic errors and the contaminating effects of the substructure on the flux ratios. Effectively we follow the procedures suggested by Mao & Schneider (1998) for modeling lenses in the presence of substructure.

For analyzing the real data (steps B1-B2 in Fig. 1) we apply our linearized analysis method from §2.1 to each lens using the best fit macro model from step #2 as the reference model ( $\mathbf{p}_0$ ) supplying the reference image positions and magnifications ( $\mathbf{x}_i^{(0)}, \mathbf{M}_i^{(0)}$ ). Given the mass scale  $b$  and surface number density  $N$  of the substructure we determine the angular radius  $r_n = (n/N)^{1/2} = (nba\Sigma_{crit}/\Sigma)^{1/2}$  inside which we expect to find  $n$  perturbing satellites. For each realization of the substructure (the  $\delta_{\alpha j}$  in Eqns. (12) and (13)) we added  $n = 10$  perturbing satellites inside radius  $r_{10}$  from each image with corrections to avoid over counting in models where the  $r_{10}$  regions of the individual images overlap. Each satellite perturbed all images, an effect which becomes important for mass scales  $b \gtrsim 0''.01$ . The model is in some senses still a “local” approximation because we assume a constant surface density near all images and we do not generate a full, global realization of the substructure distribution. The more distant satellites produce perturbations which are difficult to distinguish from changes in the macro model. We varied only the mass scale  $b$  and surface density  $\Sigma/\Sigma_c$  of the substructure using logarithmic priors for the two variables ( $P(b) \propto 1/b$  and  $P(\Sigma) \propto 1/\Sigma$ ). The tidal radius was always set to  $a = (bb_0)^{1/2}$  with  $b_0 \equiv 1''.0$ . For each value of the mass scale and the surface density, we generated  $10^5$  random realizations of the substructure. *All parameters of the macro model are reoptimized for every substructure realization* by minimizing the fit statistics in Eqns. (10) and (11) combined with any ancillary constraints like the position of the primary lens galaxy. The Bayesian likelihood distribution (Eqn. 13) is constructed by combining the likelihoods of fitting the data for lens  $j$ ,  $P(D_j|\delta_{\alpha j})$  for each of the  $\alpha = 1 \cdots 10^5$  substructure realizations made for each of the set of substructure parameters  $\mathbf{s}$ .

We tested the algorithm using Monte Carlo models following the steps A1-6 in Fig. 1. The objective of the Monte Carlo sequence is to start from the best fit macro model of each lens found in step #2 and then by adding substructure and noise generate a synthetic set of lens data which should be analogous to the real data. We start by taking the best fit model for the lens (from #2) and using its parameters and source properties as the true properties of a new Monte Carlo

model. In step A1 we randomly place  $n = 5$  perturbing satellites inside the radius  $r_5$  of each image based on the desired physical properties (mass scale  $b$ , surface density  $\Sigma$ , tidal radius  $a$ ) of the substructure.

In step A2 we use the *lensmodel* package (Keeton 2001a) to find the non-linear solutions for the new image positions and fluxes including all the substructure but keeping the macro model and source properties fixed. We used  $n = 5$  perturbing satellites per image because of limitations on the maximum number of lenses in *lensmodel*. Tests varying the number of perturbers used both to generate and analyze the data suggested that the choices have no effects on the results in the sense that any biases are small compared to the statistical uncertainties. A modest fraction of realizations for B2045+265 produced extra images. We discarded these realizations. The existence of these solutions suggests that the substructure profile shape may be constrained by the production of extra images, but an exploration of these additional parameters is beyond the scope of our current study. After adding measurement errors to the image positions, lens positions and image fluxes in step A3, we have a set of synthetic lens data that should be a realistic Monte Carlo model of the real data we started with in step #1. The remainder of the analysis is identical to that for the real data. Step A4 matches step #2 where we fit the synthetic data using only a smooth macro model to provide the reference models and images for performing the substructure analysis. Step A5 matches step B1 for the real data, where we apply our linearized substructure analysis to the noisy synthetic data and the reference model, and step A6 matches step B2 where we combine the results to estimate the Bayesian likelihood distributions for the substructure parameters.

We illustrate the ability of our linearized analysis method to correctly extract the properties of substructure in three steps. First, we examined the sensitivity of our surface density estimate  $f_{sat}$  to measurement errors. Next, we tested our ability to estimate  $f_{sat}$  when the satellite masses and structures were fixed to their true values. Finally, we tested our ability to estimate simultaneously the surface density  $f_{sat}$  and the mass scale  $b$ . In each case we generate a Monte Carlo data set consisting of a perturbed realization for each of the 7 lenses in our sample and then analyze it using the same procedures we apply to the real data.

In our first test we examine whether measurement errors can be mistaken for substructure by adding random astrometry and flux errors to the models, fitting new macro models, and then analyzing the synthetic data using our method. This is unlikely to be a serious problem for the real data because the best fit models typically have  $\chi^2 \gg N_{\text{dof}}$  when we use realistic uncertainties for the image fluxes. However, this will determine the range of  $f_{sat}$  to which we are sensitive, where the relevant scales are  $10^{-4} \lesssim f_{sat} \lesssim 10^{-3}$  for normal satellite populations and  $0.02 \lesssim f_{sat} \lesssim 0.15$  for CDM substructure. The results of two such simulations are shown in Fig. 2. The formal, one-sided 90% confidence upper bounds are  $f_{sat} \lesssim 0.004$ , although this is very conservative because we only calculated the probability over the range  $10^{-3} \leq f_{sat} \leq 1$ . The peak probability and most of the integrated probability comes from still lower satellite fractions. Lenses with highly magnified images are more sensitive to substructure and constrain  $\Sigma/\Sigma_c$  more

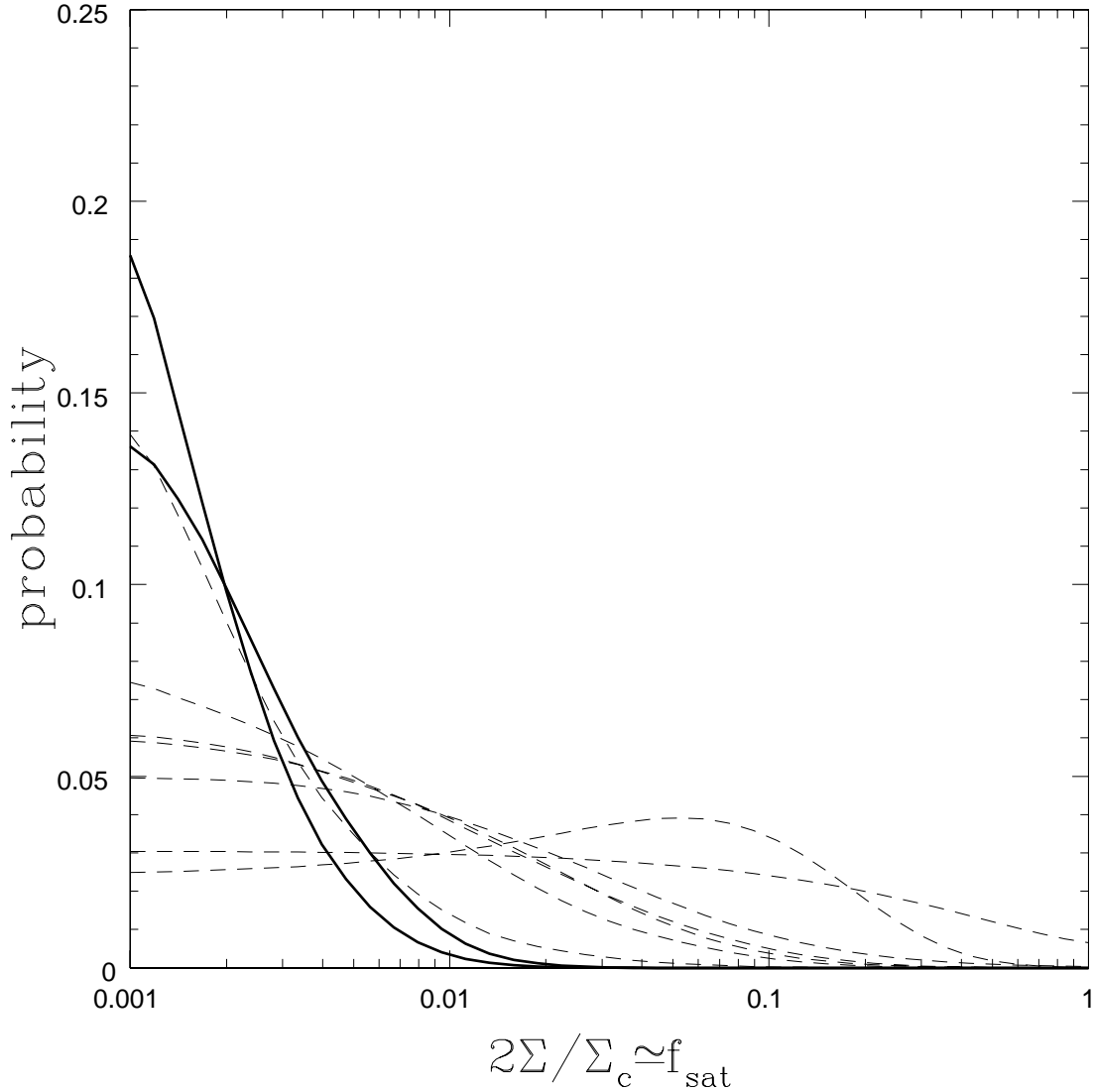


Fig. 2.— Two Monte Carlo simulations of the effects of measurement error. The dashed curves show the likelihood distribution for each lens in the first realization and the heavy solid curves show the final Bayesian probability distributions for the two realizations of 7 lenses. Our formal upper limit is  $f_{sat} \lesssim 0.004$  in both trials, but the limit would be lower had we extended the calculation beyond the range  $10^{-3} < f_{sat} < 1$ .

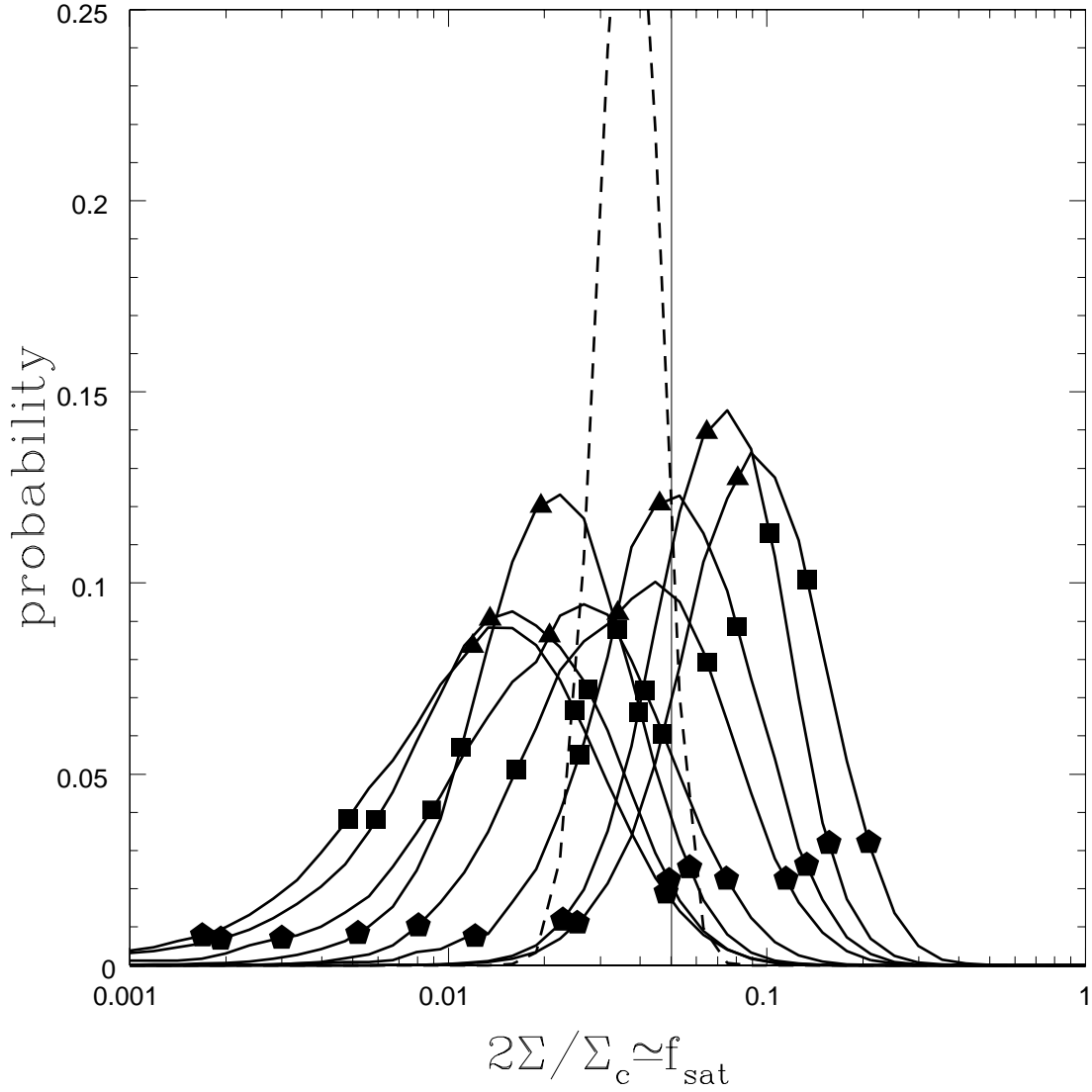


Fig. 3.— Eight Monte Carlo simulations with  $f_{sat} = 0.05$  and  $b = 0.001$ . The light dashed curves show the likelihood distribution for each lens in the first realization, the heavy solid curves show the final Bayesian probability distributions for all eight realizations of 7 lenses each, and the heavy dashed curve shows the combined probability of all 8 realizations. This latter case mimics a sample of 56 lenses. The points on the heavy curves mark the median probability (triangles) and the regions encompassing 68.3% ( $1\sigma$ , squares), and 95.4% ( $2\sigma$ , pentagons) of the likelihood in the Bayesian probability distribution. The vertical line marks the true value of  $f_{sat} = 0.05$ .

strongly, with the upper limit varying as the inverse square of the maximum image magnification. Our lens sample has two “low-magnification” lenses ( $M_{max} \lesssim 5$ , B1608+656, B1933+503) and five “high-magnification” lenses ( $M_{max} \gtrsim 5$ , MG0414+0534, B0712+472, PG1115+080, B1422+231, and B2045+265). Individual lenses can even show probability peaks at larger surface densities, but without the contrast between the peak and the probability at lower  $f_{sat}$  needed to produce a signal at higher surface density in the full sample. If, however, we underestimate the flux errors, we can make a spurious detection of the substructure. When we examine a range of satellite mass scales  $b$  as well as the surface density, we find that measurement errors produce no preferred mass scale for the substructure.

In the second set of simulations we added perturbing satellites near each image with a surface density of  $f_{sat} = 2\Sigma/\Sigma_c = 0.05$  and a mass profile defined by  $b = 0''.001$  and  $a = 0''.032$ . The radius encompassing an average of 5 satellites,  $r_5 = 0''.080$ , is much smaller than the distances between the images. We experimented with other models, but the results we present were typical. As we show in Fig. 3, the estimated surface density is consistent with the surface density used to generate the data. In the eight simulations shown in Fig. 3, the surface density corresponding to the median probability ranges from  $f_{sat} = 0.01$  to 0.08 with uncertainties of a factor of 2.5 at  $1\sigma$  and 3.0 at 90% confidence. The true surface density is within the 68.3% ( $1\sigma$ ) confidence region in 4 of the 8 simulations and within the 90% confidence region for 6 of the 8 simulations. If we combine all 8 simulations to mimic a sample of 56 lenses, the surface density estimated by the median of the Bayesian likelihood distribution is  $f_{sat} = 0.034$  with a 90% confidence range of  $0.023 \leq f_{sat} \leq 0.048$  that marginally excludes the true value. The slightly low value for  $f_{sat}$  could be due to chance, discarding the cases producing additional images, linearizing the problem or the local approximation for the substructure.

We also examined the likelihood distribution in the two-dimensional space of the surface density  $f_{sat}$  and the mass scale  $b$ , holding the internal structure of the satellites fixed with  $a = (bb_0)^{1/2}$  for  $b_0 \equiv 1''.0$ . Fig. 4 shows that the method can recover the mass scale, but less robustly than the surface density of the satellites. In these two-dimensional models we find median estimates for the surface density ranging from  $f_{sat} = 0.014$  to 0.074 with a factor of 3.8 uncertainty at 90% confidence. The ability to adjust the mass scale significantly increases the uncertainty in the surface density. The median estimates for the mass scale range from  $b = 0''.00016$  to  $0''.0027$ . The uncertainty in the mass scale is usually an order of magnitude at 90% confidence. As we discuss in §2.2, we expect to be more sensitive to the surface mass density than to the mass scale. For constant astrometry perturbations we expect  $b \propto f_{sat}^{-2/3}$  and for constant shear or convergence perturbations we expect  $b \propto f_{sat}^{-2}$  (see eqns. 17 and 18). Neither slope is clearly reflected in the likelihood contours of Fig. 4, suggesting that both types of perturbations contribute. If we combine all 8 realizations to mimic a sample of 56 lenses, we recover the input model with modest uncertainties.

In summary, the lenses are sensitive to surface densities of substructure exceeding  $f_{sat} \gtrsim 0.004$  and samples of 7 lenses can be used to determine the surface density and mass scale with

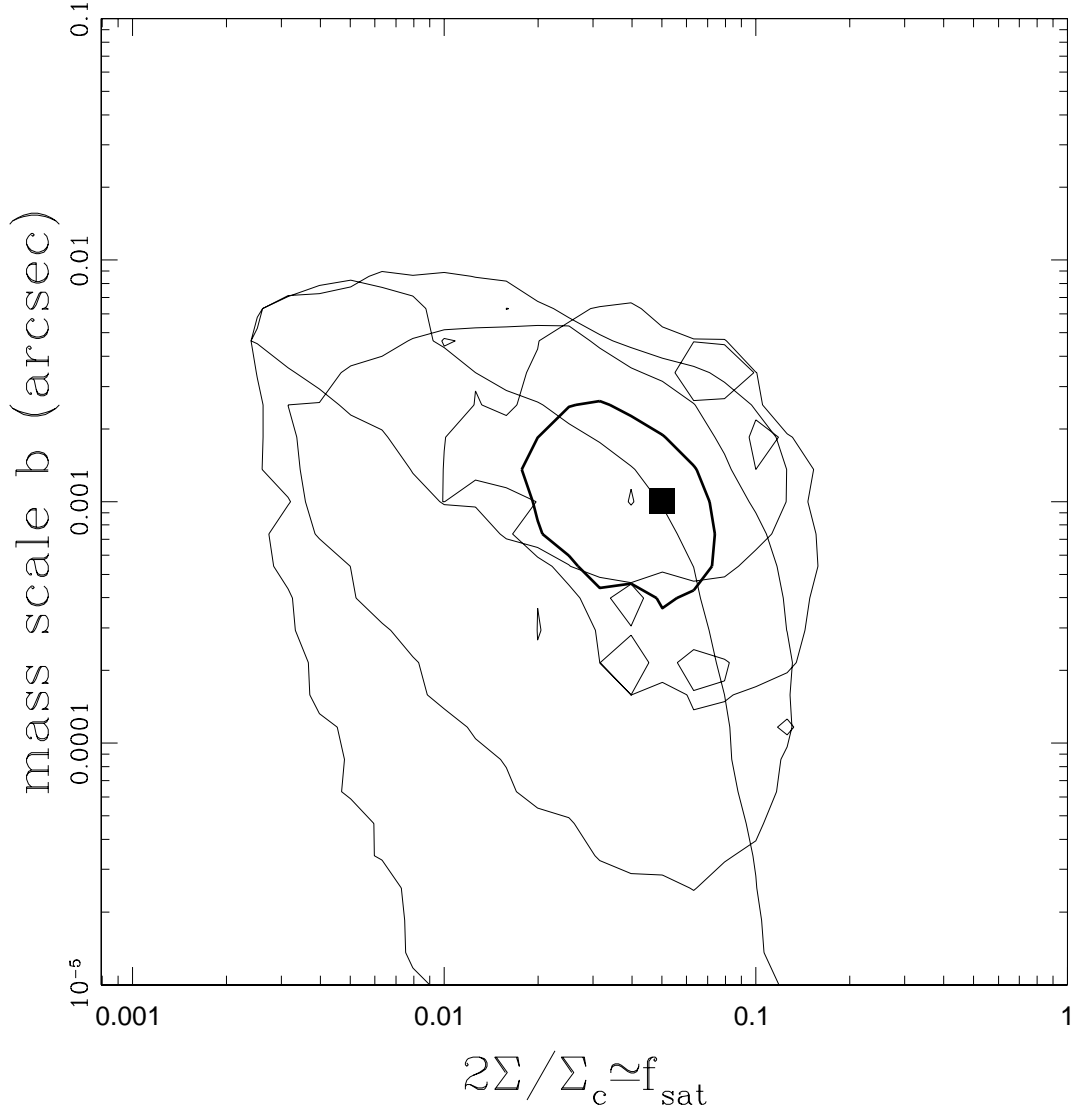


Fig. 4.— Monte Carlo simulations including both the surface density  $f_{\text{sat}}$  and the mass scale  $b$ . We show the probability contour enclosing 90% of the total probability for four of the eight models shown in Fig. 3. The heavy contour shows the result after combining all eight realizations and the solid square marks the true model parameters.

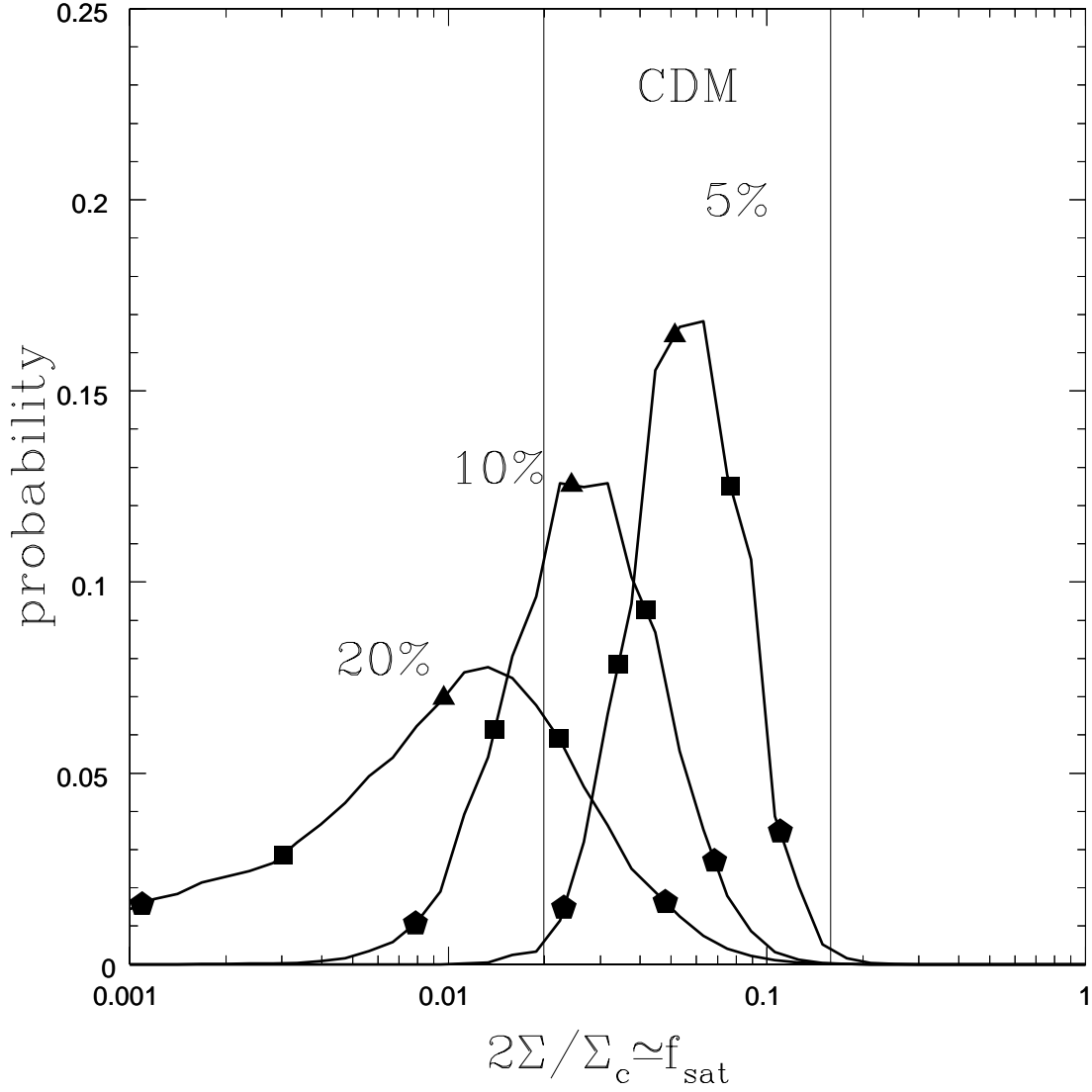


Fig. 5.— Results for the observed lens sample with  $b = 0''.001$ . The heavy solid lines show the probability distributions assuming errors in the flux ratios of 5%, 10% and 20%. The points on the curves mark the median surface density (triangles) and the regions encompassing 68.3% ( $1\sigma$ , squares), and 95.4% ( $2\sigma$ , pentagons) of the probability. The dashed curves show the contributions from the individual lenses for the 10% case. The region between the vertical lines is the range of substructure mass fractions found in the Klypin et al. (1999) simulations. Normal satellite populations, with  $10^{-4} \lesssim f_{sat} \lesssim 10^{-3}$ , correspond to a region off the left edge of the figure.

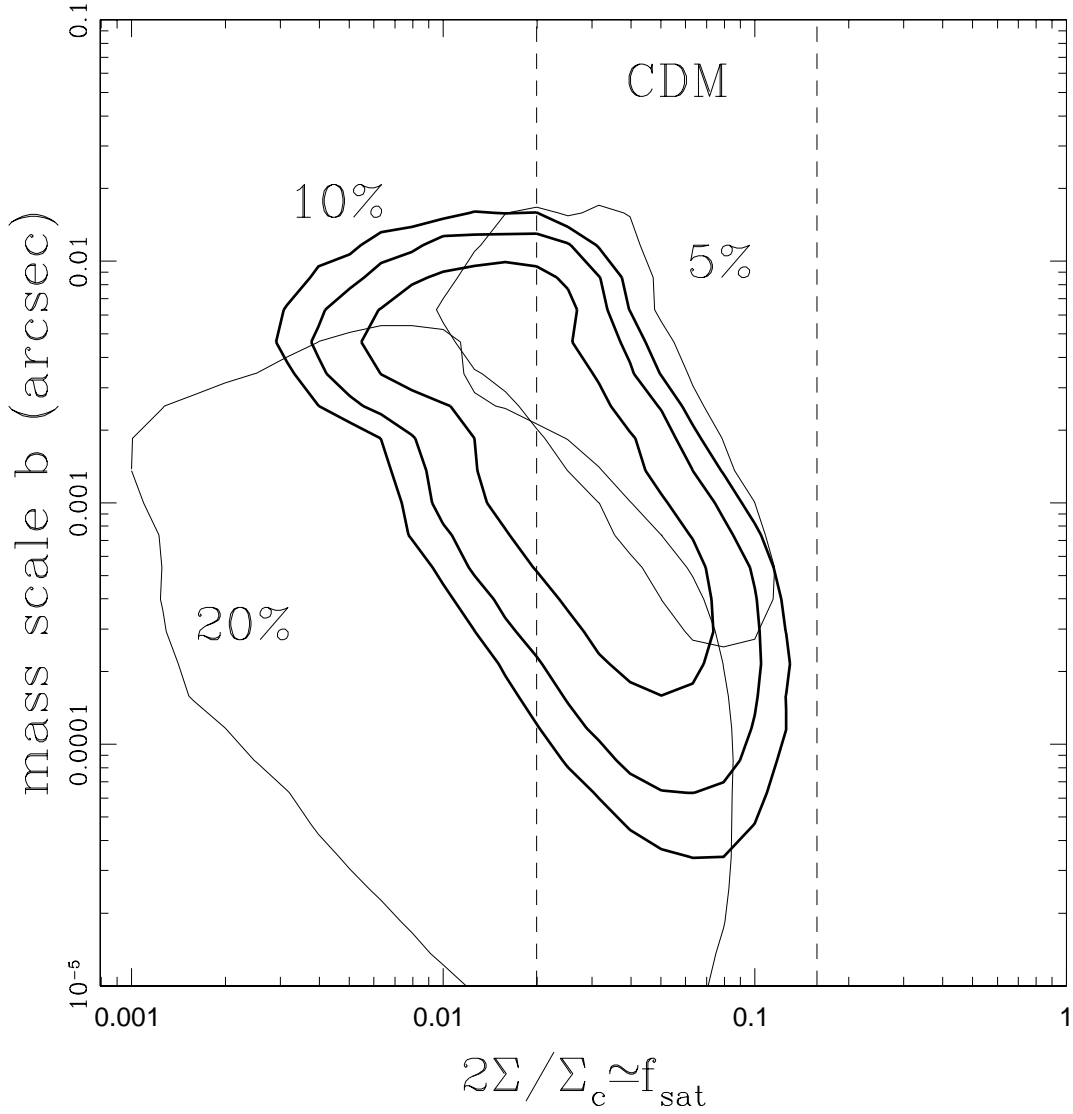


Fig. 6.— Results for the observed lens sample as a function of both the surface density  $f_{sat}$  and the mass scale  $b$ . For the case with 10% flux errors we show the probability contours enclosing 68% ( $1\sigma$ ), 90%, and 95% ( $2\sigma$ ) of the total probability using heavy solid curves. For the cases with 5% and 20% flux errors we show only the probability contour encompassing 90% of the probability using a light solid curve. The region between the vertical lines is the range of substructure mass fractions found in the Klypin et al. (1999) simulations. Normal satellite populations, with  $10^{-4} \lesssim f_{sat} \lesssim 10^{-3}$ , correspond to a region off the left edge of the figure.



reasonable accuracy. Our method shows no signs of biases in the recovered parameters given the statistical uncertainties expected for 7 lenses. In much larger lens samples, or samples with very accurately measured image fluxes, we may underestimate the surface density slightly as a consequence of the simplifications made to allow rapid calculation (linearizing the problem and the “local” approximation for the substructure) and the elimination of realizations generating extra images.

### 3. The Properties of Halo Substructure

Given these limitations we now apply the analysis to the sample of 7 real lenses. We will assume an average uncertainty in the flux ratio measurements of 10%, but report results for uncertainties of 5% and 20% as well. For the few cases where the flux measurement errors are larger we use the measurement errors instead, but in most cases the flux measurement errors are dominated by systematic uncertainties rather than measurement errors. Amongst the systematic issues are variability and time delays, wavelength dependencies to the flux ratios, and any contribution from stellar microlensing. A detailed examination of these problems is beyond the scope of our present study. Given the current data for most lenses, the image flux uncertainties are certainly lower than 20%, probably lower than 10% and unlikely to be lower than 5%. The errors in the image and lens positions are dominated by measurement errors rather than systematic errors.

We first analyzed the data assuming a fixed mass scale of  $b = 0''.001$  and a tidal radius of  $a = 0''.032$ . As shown in Fig. 5, the results for the real lens sample have qualitative properties that are very similar to the results of the Monte Carlo simulations shown in Fig. 3. The median estimate for the surface density depends on the assumed level of systematic uncertainties in the image flux ratios, with  $f_{sat} \equiv 2\Sigma/\Sigma_{crit} = 0.051, 0.024$  and  $0.0097$  for flux ratio uncertainties of 5%, 10% and 20% respectively. The 90% confidence ranges for the three cases are  $0.027 < f_{sat} < 0.096$ ,  $0.0098 < f_{sat} < 0.058$  and  $0.0014 < f_{sat} < 0.037$  respectively. In all three cases the distributions are broadly consistent with the  $0.02 < f_{sat} < 0.15$  range found in the Klypin et al. (1999) simulations, and well above the  $10^{-4} \lesssim f_{sat} \lesssim 10^{-3}$  found in visible satellites (see Mao & Schneider 1998, Chiba 2001).

We also calculated the probabilities as a function of both  $f_{sat}$  and the mass scale  $b$  as shown in Fig. 6. With 10% flux errors the median estimates for the surface density and mass scale are  $f_{sat} = 0.020$  and  $0''.0013$  with 90% confidence regions of  $0.0058 < f_{sat} < 0.068$  and  $0''.0001 < b < 0''.007$ . For a  $dn/dM \propto 1/M^2$  ( $M_{low} < M < M_{high}$ ) satellite mass function this implies that the upper mass scale is in a range  $10^6 M_{\odot} \lesssim M_{high} \lesssim 10^9 M_{\odot}$  that is consistent with the expectations for satellites. There is a relatively strong covariance between the parameters  $b$  and  $f_{sat}$ , with low surface densities requiring higher mass scales. The slope of the likelihood contours is very close to the  $b \propto f_{sat}^{-2}$  slope corresponding to constant shear or convergence perturbations (see eqn. 18) rather than the flatter  $b \propto f_{sat}^{-2/3}$  slope corresponding to constant

astrometry perturbations (see eqn. 17). If we assume 5% flux errors, then the surface density and mass scales are restricted to larger values, with  $0.013 \lesssim f_{sat} \lesssim 0.078$  and  $0''.00036 \lesssim b \lesssim 0''.013$ . If we assume 20% flux errors, a broader range is permitted, with  $0.0016 \lesssim f_{sat} \lesssim 0.051$  and  $0''.000015 \lesssim b \lesssim 0''.0023$ . These calculations neglect the smoothing effects of the finite source size ( $\Delta\theta \sim 0.01\text{--}1.0$  milliarcsecond), which will wash out the perturbations from smaller satellites if  $\Delta\theta \gtrsim b$ . With a finite source size, we would require a larger satellite fraction to produce the same perturbations to the images. On a final, if qualitative note, the general properties of the likelihood distributions for the real data are remarkably similar to those of the Monte Carlo simulations.

#### 4. Discussion

CDM simulations generically produce halos in which  $\sim 2\text{--}15\%$  of the mass is comprised by substructure, which is 50-100 times more mass than is observed in the satellites of the Local Group (e.g. Moore et al. 1999, Klypin et al. 1999). This substructure problem, and possible conflicts between rotation curves and density cusps and the observed and predicted angular momentum distributions in spiral galaxies have been interpreted as requiring significant modifications to the CDM paradigm (e.g. Spergel & Steinhardt 2000, Bode et al. 2001, Colin et al 2000).

Here we show that the anomalous flux ratios observed in a sample of 7 gravitational lenses can be interpreted as requiring a mass fraction of  $0.006 < f_{sat} < 0.07$  (90% confidence) in satellite halos that is remarkably consistent with the CDM predictions. This estimate assumed 10% errors (measurement + systematic) in the estimates of image fluxes, but the predicted surface density remains consistent with the expectations for CDM over the plausible 5-20% range for these uncertainties. The estimates are always well above the  $10^{-4} \lesssim f_{sat} \lesssim 10^{-3}$  predicted for known satellite populations (see Mao & Schneider 1998, Chiba 2001). This can be consistent with CDM and the lower density of Galactic satellites if star formation is suppressed in most such satellites as already discussed by Klypin et al. (1999) and Bullock et al. (2000). For the  $dn/dM \propto M^{-1.8}$  ( $M_{low} < M < M_{high}$ ) mass function expected for satellites (e.g. Moore et al. 1999, Klypin et al. 1999) our test provides a rough estimate of the upper mass scale  $M_{high} \simeq 10^6\text{--}10^9 M_{\odot}$ . While this is uncomfortably close to the masses capable of disrupting stellar disks and globular clusters (e.g. Moore et al. 1999), Font et al. (2001) find that the expected CDM substructure is consistent with the survival of thin galactic disks. Thus, our result confirms a surprising if generic prediction of CDM models and can be regarded as a major success of the CDM model. By the same token, alternatives to CDM which aim to suppress small-scale power (warm dark matter) or to destroy small satellites (self-interacting dark matter) are accordingly disfavored.

We believe that three other explanations, systematic errors in the data, unmodeled, coherent structures in the lens and stellar microlensing, are unlikely. While there are systematic errors in the lens data, the anomalous flux ratios which drive the detection of substructure are present at levels far above the measurement errors and appear in multiple observations at differing wavelengths over periods of years. They may be misinterpreted but not eliminated. They are also unlikely

to be due to coherent structures in the lens galaxy. While we analyzed the lenses using singular isothermal ellipsoids in an external shear for the macro model, Metcalf & Zhao (2002) have shown that the flux ratios cannot be explained by a broad range of macro models. The typical lens galaxy, including all seven discussed here, is an early-type galaxy whose surface brightness profile is well modeled by a smooth, elliptical de Vaucouleurs profile (e.g. Lehar et al. 2000, Kochanek et al. 2000) with no obvious photometric residuals. Coherent features in the lenses like spiral arms would be trivially detected in most cases. Moreover, if we need  $f_{sat} \sim 0.01$  in compact components like satellites to perturb the images, we would require a far bigger mass fraction in large scale, coherent structures that cannot produce perturbations isolated to a single image.

The most problematic alternative explanation is stellar microlensing, which is the same physical phenomenon but produced by the stellar populations we know to be present in the lens galaxy. The basic argument against microlensing is that it has too small a characteristic angular scale ( $\mu\text{as}$ =microarcseconds) to produce large, long-lived flux ratio anomalies given the sizes of typical radio sources. The Compton limit, and direct VLBI observations the lenses, mean that typical sources are resolved on scales of 10–1000 $\mu\text{as}$  that are large enough to suppress the effects of stellar microlensing. The one apparent case of microlensing a radio source, B1600+434, is probably due to a superluminal sub-component of the radio source where Doppler boosting gives the source a smaller effective size and a rapid modulation time scale (see Koopmans & de Bruyn 2000). Even in B1600+434, microlensing provides only a  $\sim 5\%$  rms variation in the fluxes. Moreover, many of the radio lenses also have constant flux ratios on long time scales (years) which are difficult to reconcile with producing flux ratio anomalies using the stars. Finally, our method provides an estimate for the characteristic mass scale which is grossly inconsistent with stellar microlensing. This is reinforced by detailed analyses of B1422+231 (Keeton 2002, Bradac et al. 2002) which find mass scales compatible with CDM substructure but not stellar microlensing. In summary, satellites are the most natural explanation, and the required densities are comparable to that expected in CDM and higher than that observed in normal satellite populations. The lenses cannot address directly whether they are dark or luminous because of the enormous distances.

Our examination of the problem is a preliminary one, and our estimates can be extended and improved if the following points are addressed. First, the entire question of the image fluxes and their uncertainties needs to be carefully reconsidered. We used a fixed measurement error of 10% for the image fluxes, but the estimated surface density and its uncertainties are affected by differences between the true errors and the errors used in the analysis. Until now there has been little motivation for determining image flux ratios with high precision (say 1% accuracy), but improved analyses will need such high precision. Lens monitoring and time delay measurements, already important for using the lenses to determine the Hubble constant without the systematic problems of the local distance scale (e.g. Schechter 1999), are needed to eliminate the effects of source variability on the flux ratios. In optical lenses, observations over a broad range of wavelengths are needed to provide accurate corrections for extinction (see Falco et al. 1999).

Second, improved observations of the lenses are needed. The lensed images of the host

galaxies of the radio sources, which are relatively easy to observe using deep infrared imaging with HST, can be used to constrain the macro model (e.g. Kochanek, Keeton & McLeod 2001). Unlike the unresolved images of quasars or the marginally resolved images of radio cores, large lensed structures like the host galaxies ( $\Delta\theta \gtrsim 0''.1$ ) constrain the macro model without being affected by substructure. Combining the large scale constraints with the compact images allows us to probe the substructure while limiting the ability of the macro model to mask its effects. Simultaneously, very high resolution, high dynamic range VLBI observations to map thin, extended radio structures can be used to extend the search for substructure over larger regions in each lens (e.g. Wambsganss & Paczynski 1992, Metcalf & Madau 2001). If the VLBI observations can show that the anomalous flux ratios are consistent with the geometric structure of the image, then we can completely rule out microlensing as an alternative explanation. Finally, careful searches for additional, but faint, VLBI images produced by the substructure may be a powerful means to constrain the density profiles of the satellites. We have already found that our assumed density satellite profile occasionally produces additional, detectable images, suggesting that a shallower density profile would be preferred.

Third, the analysis can be expanded to include complete treatments of the mass spectrum, the density profiles of the substructure and the effects of finite sized sources. These additional complications were unwarranted in this first calculation because with only 7 lenses all we can realistically say we have measured are the average properties of the substructure. Any model producing the same average shear and astrometry perturbations should be consistent with the data. It is clear from our Monte Carlo simulations, where our model would occasionally generate additional images, that the density distribution of the more massive substructures can be constrained by limits on the production of extra images. Given our estimated angular scales for the substructure perturbations and the dominance of the mass spectrum by the higher mass halos, our effects should be little affected by finite source sizes. If the typical radio source is 1 mas, then we are modestly underestimating the surface density.

Finally, larger samples of lenses can reduce the considerable Poisson uncertainties. At least two additional radio quads have been discovered (B0128+437, Phillips et al. 2000; and B1555+375 Marlow et al. 1999) in the CLASS survey we used as the basis for our analysis, but lack the HST imaging data needed to accurately determine the position of the lens galaxy. Two-image lenses, while less optimal because of their lower average magnifications, can be included in the analysis when additional lensed structures like the images of the quasar host galaxy or VLBI subcomponents provide the constraints needed to break the degeneracies between the macro model and the substructure we expect for a simple two-image lens.

Lastly, we note that other probes of substructure may be possible in Local Group galaxies. Very recently, Ibata et al. (2001a, 2001b) have suggested that the paucity of tidal streamers in the Milky Way halo may betray the presence of halo substructure. Johnston et al. (2001) similarly analyze tidal debris from the disrupted Sagittarius dwarf, and find that stars in these tidal tails appear to be more scattered than expected for debris orbiting in a smooth halo. Thus there are

tantalizing hints of evidence for substructure within our own halo, and further work along this avenue may lead to more definite conclusions than is presently possible. Whatever the outcome of these local studies, however, only gravitational lenses can detect directly CDM satellites in which star formation was suppressed.

### Acknowledgments

We thank David Rusin, Josh Winn and Stuart Wyithe for many helpful discussions. We also thank Charles Keeton and David Rusin for making their lensing codes available, and Joanne Cohn for suggesting ND visit SAO. CSK was supported by the Smithsonian Institution and NASA grants NAG5-8831 and NAG5-9265. ND was supported by the Smithsonian Institution Short Term Visitor Program, the Dept. of Energy under grant DOE-FG03-97-ER 40546, and the ARCS Foundation.

### REFERENCES

- Biggs, A.D., Xanthopoulos, E., Browne, I.W.A., Koopmans, L.V.E., & Fassnacht, C.D., 2000, MNRAS, 318, 73
- Bode, P., Ostriker, J. P. and Turok, N. 2001, ApJ, 556, 93
- Bradac, M., Schneider, P., Steinmetz, M., Lombardi, M., & King, L.J., 2002, A&A submitted, astro-ph/0112038
- Bullock, J. S., Kravtsov, A. V. and Weinberg, D. H. 2000, ApJ, 539, 517.
- Chiba, M., 2001, astro-ph/0109499
- Chiu, W.A., Gnedin, N.Y., & Ostriker, J.P., 2001, astro-ph/0103359
- Cohn, J.D., Kochanek, C.S., McLeod, B.A., & Keeton, C.R., 2001, ApJ, 554, 1216
- Colin, P., Avila-Reese, V., & Valenzuela, O., 2000, ApJ, 542, 622
- Falco, E.E., Impey, C.D., Kochanek, C.S., Lehar, J., McLeod, B.A., Rix, H.-W., Keeton, C.R., Munoz, J.A., Peng, C.Y., 1999, ApJ, 523, 617
- Fassnacht, C.D., Womble, D.S., Neugebauer, G., Browne, I.W.A., Readhead, A.C.S., Matthews, K., & Pearson, T.J., 1996, ApJL, 460, 103
- Fassnacht, C.D., Blandford, R.D., Cohen, J.G., et al., 1999, AJ, 117, 658
- Font, A.S., Navarro, J.F., Stadel, J., & Quinn, T., 2001, astro-ph/0106268

- Helmi, A., White, S.D.M., & Springel, V., 2002, astro-ph/0201289
- Hewitt, J.N., Turner, E.L., Lawrence, C.R., Schneider, D.P., & Brody, J.P., 1992, AJ, 104, 968
- Ibata, R. A., Lewis, G. F., and Irwin, M. J. 2001a, astro-ph/0110690
- Ibata, R. A., Lewis, G. F., Irwin, M. J., and Cambresy, L. 2001b, astro-ph/0110691
- Jackson, N., Nair, S., Browne, I.W.A., et al., MNRAS, 296, 483
- Johnston, K. V., Spergel, D. N., and Haydn, C. 2001, astro-ph/0111196
- Kauffmann, G., White, S.D.M., & Guiderdoni, B., 1993, MNRAS, 264, 201
- Keeton, C., 2002, ApJL submitted, astro-ph/0111595
- Keeton, C. 2001, ApJ submitted, astro-ph/0102340
- Keeton, C. 2001, ApJ submitted, astro-ph/0105200
- Klypin, A., Kravtsov, A.V., Valenzuela, O., & Prada, F., 1999, ApJ, 522, 82.
- Kochanek, C.S., Keeton, C.R., & McLeod, B.A., 2001, ApJ, 547, 50
- Kochanek, C.S., 2001, The Dark Universe, M. Livio, ed., (Cambridge: Cambridge Univ. Press)  
(also astro-ph/0108160)
- Kochanek, C.S., Falco, E.E., Impey, C.D., Lehar, J., McLeod, B.A., Rix, H.-W., Keeton, C.R.,  
Munoz, J.A., & Peng, C.Y., 2000, ApJ, 543, 131
- Koopmans, L.V.E., & de Bruyn, A.G., 2000, A&A, 358, 793
- Lehar, J., Falco, E.E., Kochanek, C.S., McLeod, B.A., Munoz, J.A., Impey, C.D., Rix, H.-W.,  
Keeton, C.R., & Peng, C.Y., 2000, ApJ, 536, 584
- Mao, S., & Schneider, P., 1998, MNRAS, 295, 587
- Marlow, D.R., Myers, S.T., Rusin, D., et al., 1999, ApJ, 188, 654
- Metcalf, R.B., & Zhao, H., ApJL submitted, astro-ph/0111427
- Metcalf, R.B., & Madau, P., 2001, astro-ph/0108224
- Moore, B. Ghigna, S., Governato, F., Lake, G., Quinn, T., Stadel, J., & Tozzi, P., 1999, ApJ, 524,  
L19
- Moore, C.B., & Hewitt, J.N., 1997, ApJ, 491, 451
- Munoz, J.A., Kochanek, C.S., & Keeton, C.R., 2001, ApJ, 558, 657

- Patnaik, A.R., Browne, I.W.A., Walsh, D., Chaffee, R.H., & Foltz, C.B., 1992, MNRAS, 254, 655P
- Phillips, P.M., Norbury, M.A., Koopmans, L.V.E., et al., MNRAS, 319, L7
- Schechter, P., 1999, New Cosmology and the Values of the Fundamental Parameter, IAU 201, eds. A.N. Lasenby and A. Wilkinson, (PASP), astro-ph/0009048
- Schneider, P., Ehlers, J., & Falco, E.E., 1992, Gravitational Lenses, (Springer Verlag: Berlin)
- Scoccimarro R., Sheth R.K., Hui L., Jain, B., 2001, ApJ, 546, 20
- Spergel, D. N. and Steinhardt, P. J. 2000, PRL, 84, 3760
- Springel, V., White, S.D.M., Tormen, G., & Kauffmann, G., 2001, MNRAS, 328, 726
- Sykes, C.M., Browne, I.W.A., Jackson, N.J., et al., 1998, MNRAS, 301, 310
- Wambsganss, J., 2001, Sources & Scintillations, IAU182, astro-ph/0012423
- Wambsganss, J., & Paczynski, B., 1992, ApJ, 397, L1
- Weymann, R.J., Latham, D., Roger, J., Angel, P., Green, R.F., Liebert, J., Turnshek, D.A., Turnshek, D.E., & Tyson, J.A., 1980, Nature, 285, 641